Sharp cell type boundaries emerge from coordinated morphogen signaling

Ruiqi Li,[1,2,14] Yiqun Jiang,[3,4,14] Sarah Platt,[3,14] Tianchi Xin,[5] Shagun Lukkad,[3] Sarah Van,[3] Kevin A. Peterson,[6] Ryan Driskell,[7] Jonathan Zhu,[3] Hainan Lam,[3] Eva-LaRue Barber,[3] David H. Wang,[8,9] Chae Ho Lim,[10,11] Makoto Mark Taketo,[12] Yuval Kluger,[1,2,13] and Peggy Myung[2,3,4]

[1]Computational Biology and Biomedical Informatics Program, Yale University, New Haven, Connecticut 06520, USA; [2]Department of Pathology, Yale University, New Haven, Connecticut 06520, USA; [3]Department of Dermatology, Yale University, New Haven, Connecticut 06520, USA; [4]Molecular, Cellular, and Developmental Biology Program, Yale University, New Haven, Connecticut 06520, USA; [5]Department of Genetics, Yale University, New Haven, Connecticut 06520, USA; [6]The Jackson Laboratory, Bar Harbor, Maine 04609, USA; [7]School of Molecular Biosciences, Washington State University, Pullman, Washington 99164, USA; [8]Department of Internal Medicine, University of Michigan, Ann Arbor, Michigan 48109, USA; [9]Medical Service, Veterans Administration Ann Arbor Healthcare System, Ann Arbor, Michigan 48105, USA; [10]Ronald O. Perelman Department of Dermatology, New York University Grossman School of Medicine, New York, New York 10016, USA; [11]Department of Cell Biology, New York University Grossman School of Medicine, New York, New York 10016, USA; [12]Colon Cancer Project, Graduate School of Medicine, Kyoto University, Sakyo, Kyoto 606-8501, Japan; [13]Department of Applied and Computational Mathematics, Yale University, New Haven, Connecticut 06511, USA

Classic models of the French flag problem depict sharp cell type boundaries emerging from threshold responses to morphogen gradients. How discrete cell type boundaries arise from morphogen signals that vary continuously across developing tissues remains incompletely understood. We use hair follicle dermal condensate (DC) formation to study a sharp developmental transition in which proliferative progenitors undergo cell cycle exit concurrent with molecular differentiation. Using genetic and genomic approaches, we show that Wnt and Hedgehog signaling coordinate separable cellular events during DC commitment. Elevated Wnt signaling promotes cell cycle exit through reduced chromatin binding of the Hedgehog mediator GLI3, while Hedgehog signaling induces differentiation genes in a Wnt-dependent manner and simultaneously elevates Wnt activity. When these responses coincide, differentiation and cell cycle exit occur together, limiting the duration and abundance of intermediate states and producing a sharp boundary. When they do not, intermediate states persist and expand, producing a graded boundary. Thus, a sharp boundary can emerge from a continuous transition that is compressed in time and space.

[*Keywords*: dermis; Hedgehog; morphogen; patterning; Wnt; scRNA sequencing]

Supplemental material is available for this article.

Received April 2, 2026; revised version accepted July 22, 2026.

Developing tissues must organize distinct cell types across space and time to assemble functional organs. Lewis Wolpert framed this problem as the "French flag" problem, in which discrete cell types emerge at defined positions along a morphogen gradient (Fig. 1A; Wolpert 1969). In this framework, graded morphogen signals are interpreted through concentration thresholds that delineate spatial domains of cell fate (Driever and Nusslein-Volhard 1988; Roelink et al. 1995; Benzinger and Briscoe 2025). However, a fundamental question remains unresolved: how sharp cell type boundaries emerge in vivo when the underlying signals and cell states vary continuously across a tissue. In many developing systems, boundaries do not arise from instantaneous fate switches. Instead, cells progress through dynamic transitions and pass through intermediate states before committing to a new identity. In many mammalian tissues, these transitions unfold while cells continue to proliferate, raising the question of how ongoing cell cycle dynamics are coordinated with graded morphogen inputs. Thus, boundary sharpness may reflect not only where thresholds are crossed, but how rapidly cells traverse a shared developmental progression.

Addressing the temporal dimension of the French flag problem has been challenging, because existing approaches typically capture either cell origins and end points or cell behaviors, making it difficult to resolve intermediate

[14]These authors contributed equally to this work.
Corresponding author: peggy.myung@yale.edu
Article published online ahead of print. Article and publication date are online at http://www.genesdev.org/cgi/doi/10.1101/gad.353815.126. Freely available online through the *Genes & Development* Open Access option.

© 2026 Li et al. This article, published in *Genes & Development*, is available under a Creative Commons License (Attribution-NonCommercial 4.0 International), as described at http://creativecommons.org/licenses/by-nc/4.0/.

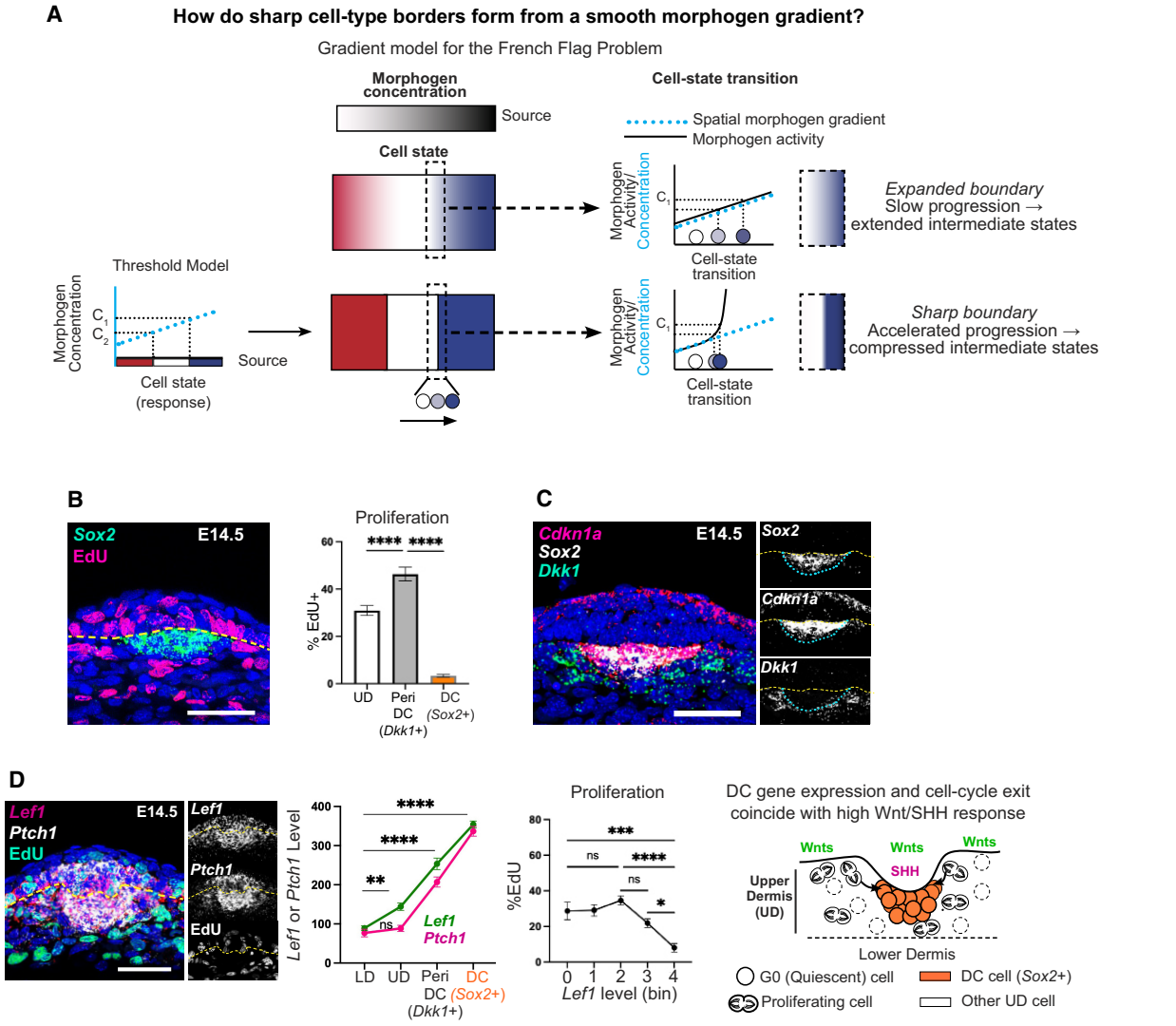


Figure 1. Cell cycle exit and molecular differentiation are temporally coordinated during dermal condensate formation. (*A*) Schematic of the French flag problem, showing how gradual versus accelerated cell-state transitions can produce expanded versus sharp boundaries in a fixed morphogen gradient. (*B*) FISH of E14.5 skin showing *Sox2*/EdU and quantification of EdU incorporation in upper interfollicular dermis (UD), *Dkk1*$^+$ peri-DC, and DC regions ($n = 10$). (*C*) FISH showing *Cdkn1a* expression in *Sox2*$^+$ DC cells adjacent to *Dkk1*$^+$ peri-DC cells ($n = 10$). (*D*) E14.5 FISH and quantification of *Lef1* and *Ptch1* levels by dermal region and EdU incorporation by *Lef1* bin. (*Right*) Schematic summary. Yellow dashed lines mark the epidermal–dermal boundary ($n = 5$). Quantifications include eight follicles or regions per embryo from three to four embryos unless otherwise indicated. Data are mean ± SEM; one-way ANOVA. (ns) Not significant. Scale bars, 50 µm.

cell states during an ongoing transition (Rompolas et al. 2012; Ouspenskaia et al. 2016; Mok et al. 2019; Morita et al. 2021). We address this problem in a mammalian system by examining hair follicle dermal condensate formation, a tractable developmental transition in which the principal morphogen signals are known and cell-state progression occurs over a narrow temporal window (Huh et al. 2013; Glover et al. 2017; Gupta et al. 2019; Qu et al. 2022).

Dermal condensates (DCs) are clusters of quiescent dermal cells that form beneath epithelial hair follicle placodes and are essential for hair follicle development (Chase et al. 1951; Hardy 1992; Millar 2002). At E13.5, prior to DC formation, Wnt signaling is broadly activated across the upper dermis in response to epidermal Wnt ligands, forming a gradient that is highest in cells closest to the epidermis (Zhang et al. 2009; Chen et al. 2012; Gupta et al. 2019). This Wnt response is required but not sufficient for DC formation. Upon placode formation, placode epithelial cells secrete Sonic Hedgehog (SHH) and additional Wnt ligands, resulting in localized coactivation of Wnt and SHH in underlying dermal cells (St-Jacques et al. 1998; Chiang et al. 1999; Gritli-Linde et al. 2007; Woo et al. 2012). Together, these signals are necessary and sufficient for DC formation (Qu et al. 2022). However, DC formation occurs as a sharp transition with few detectable intermediates. Thus, how Wnt and SHH signaling interact to produce this seemingly discrete transition

remains unclear (Glover et al. 2017; Gupta et al. 2019). This raises the question of whether the abrupt appearance of DCs reflects a single, indivisible transition or separable cellular events that are normally synchronized in vivo.

Previous work has examined how tissue growth and proliferation affect morphogen gradients by shaping field size, ligand distribution, or the scaling of positional information (Lander et al. 2002; Gregor et al. 2007; Kicheva et al. 2012). In these models, proliferation is typically considered in terms of how it modifies the signaling environment cells interpret. However, many mammalian tissues undergo differentiation while cells continue to divide, introducing an additional constraint, as proliferative expansion of intermediate states may influence the precision of pattern formation (Clevers 2013; Gao et al. 2014; Sun et al. 2023). Here, we examine how interacting morphogen signals coordinate cell cycle exit with differentiation to limit the expansion of intermediate states and ensure precise spatial patterning in proliferative tissues.

Combining in vivo genetic perturbations, chromatin profiling, and a single-cell computational framework that disentangles concurrent biological programs, we capture intermediate states that are normally difficult to detect and determine how their timing and spatial extent are regulated by Wnt and SHH signaling in vivo (Qu et al. 2024). We show that Wnt and SHH differentially regulate cell cycle exit and differentiation, and that their temporal coordination determines whether intermediate states are compressed or expanded, thereby controlling boundary sharpness. Mechanistically, we identify cross-regulation of transcription factor chromatin occupancy as a key mechanism linking signaling dynamics to cell cycle exit.

Results

Cell cycle exit and molecular differentiation are temporally coordinated during dermal condensate formation

Classic models of the French flag problem propose that distinct cell states are specified by threshold levels of morphogen concentration that vary with distance from a polarized source, predicting that sharp cell type boundaries arise from spatial differences in morphogen signaling (Fig. 1A). To examine how this model applies to hair follicle dermal condensate (DC) formation, we asked how dermal cell states are spatially organized before and during DC formation. Prior to DC formation, dermal cells are proliferative and lack DC-specific markers (Supplemental Fig. S1A). Upon DC formation, DC cells express characteristic differentiation markers, including *Sox2*, *Sox18*, and *Gal*, and show minimal EdU nucleotide incorporation, while neighboring upper dermal cells do not express DC genes and remain highly proliferative. (Fig. 1B,C; Supplemental Fig. S1B,C).

Using in vivo labeling, we previously showed that DC cells arise from highly proliferative progenitors located in the upper dermis at E13.5 (Gupta et al. 2019; Qu et al. 2022). As DC formation initiates, proliferating cells that give rise to DCs are localized to a region surrounding the nascent condensate (peri-DC region) where they express *Dkk1* (Fig. 1C; Supplemental Fig. S1C; Qu et al. 2022). *Dkk1*$^+$ peri-DC cells occupied the border between proliferative upper dermis and *Sox2*$^+$ DC cells, consistent with a transitional state. In contrast, DC marker expression overlapped with the in vivo G1/G0 Fucci2 reporter and with expression of the cell cycle inhibitor *Cdkn1a* (*p21*), with only rare *Cdkn1a*$^+$ cells lacking *Sox2* (Fig. 1C; Biggs et al. 2018; Gupta et al. 2019). These data indicate that cell cycle exit and DC differentiation are tightly associated during DC formation.

Given this temporal coincidence, we next asked how these two processes relate to Wnt and Sonic Hedgehog (SHH) signaling during DC formation. At E13.5, prior to SHH expression, Wnt signaling is active in the upper dermis (Supplemental Fig. S1A) but is not sufficient to induce DC gene expression (Zhang et al. 2009; Chen et al. 2012; Gupta et al. 2019). Using *Lef1* as a canonical readout of Wnt activity, which is concordant with expression of multiple Wnt target genes (e.g., *Axin2*, *Wif1*, *Tcf7*) (Gupta et al. 2019; Qu et al. 2022), we examined the relationship between Wnt signaling and proliferation. At E13.5, *Lef1* expression was highest in the most superficial layer of the dermis and decreased across deeper dermal cell layers, yet this spatial pattern did not correlate with EdU incorporation, nor with DC gene expression (Supplemental Fig. S1A).

By E14.5, SHH expression in placode cells coincided with SHH pathway activation in the underlying dermis. At this stage, dermal SHH activity (assessed by *Ptch1*) covaried with Wnt signaling (*Lef1*) across dermal populations, with significantly higher *Lef1* levels detected compared to E13.5 (Fig. 1D). The highest levels of both signals were observed in DC cells, intermediate levels in peri-DC (*Dkk1*$^+$) cells, and progressively lower levels in surrounding upper dermal cells. In contrast to E13.5, elevated Wnt activity at E14.5 correlated with reduced proliferation, with the lowest EdU incorporation observed in DC cells (Fig. 1D). Thus, quiescence and molecular differentiation coincide spatially and temporally within a narrow domain characterized by elevated Wnt and SHH signaling.

Elevated Wnt activity induces cell cycle exit without DC differentiation

To examine how Wnt and SHH signaling contribute to the pre-DC-to-DC transition, we perturbed each pathway prior to DC formation. Because both pathways are required for DC differentiation, loss-of-function approaches preclude analysis of their individual roles at this stage (St-Jacques et al. 1998; Chiang et al. 1999; Chen et al. 2012; Gupta et al. 2019; Qu et al. 2022). As DC cells ultimately exhibit the highest levels of both Wnt and SHH activity, we asked whether these signals contribute to distinct components of the transition or act through a shared mechanism. We therefore elevated Wnt signaling before DC formation by expressing constitutively activated β-catenin (*Axin2CreER;βcat*$^{fl/EX3}$, referred to here as Actβcat) (Fig. 2A, tamoxifen at E11.5).

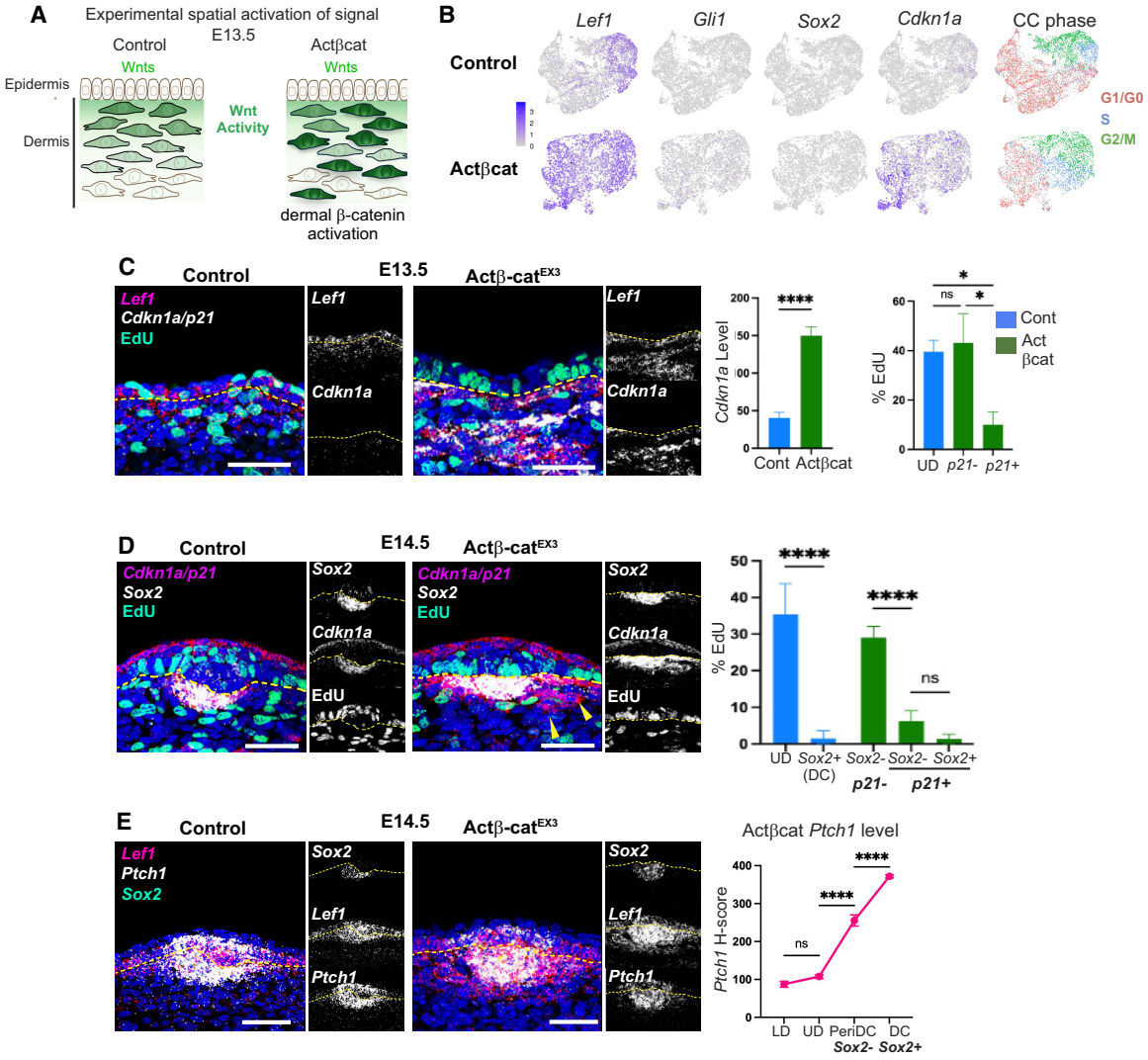


Figure 2. Elevated Wnt activity induces cell cycle exit without DC differentiation. (*A*) Experimental design for constitutive dermal β-catenin activation before DC formation (tamoxifen E11.5). (*B*) E13.5 Actβcat mutant and control dermal scRNA-seq UMAPs colored by indicated genes or cell cycle phase ($n = 2$). (*C*) E13.5 *Lef1*, *Cdkn1a*, and EdU FISH and quantification of *Cdkn1a* levels and the percentage of EdU incorporation in *Cdkn1a*– and *Cdkn1a*$^+$ upper dermal cells ($n = 3$). (*D*) E14.5 *Sox2*, *Cdkn1a*, and EdU FISH with quantification of the percentage of EdU$^+$ cells in the indicated control or Actβcat populations ($n = 5$). (*E*) E14.5 *Lef1*, *Ptch1*, and *Sox2* FISH and quantification of *Ptch1* levels in Actβcat by cell type ($n = 3$). Yellow dashed lines mark the epidermal–dermal boundary. Quantifications include six to eight follicles or regions per embryo from three to four embryos unless otherwise indicated. Data are mean ± SEM; one-way ANOVA. (ns) Not significant. Scale bars, 50 µm.

To assess how increased Wnt activity alters dermal transcriptional states prior to DC differentiation, we performed single-cell RNA sequencing of E13.5 Actβcat and control dermis. Dermal cells were filtered using established markers (e.g., *Col1a1* and *PDGFRα*). Consistent with prior work, Actβcat mutant dermal cells showed increased expression of Wnt targets (e.g., *Lef1*, *Axin2*, and *Tcf7*), but not DC markers (e.g., *Sox2*, *Gal*, and *Foxd1*) or SHH targets (e.g., *Gli1*) (Fig. 2B; Supplemental Fig. S2A, B). Notably, *Cdkn1a*, a cell cycle inhibitor normally expressed in DC cells at E14.5, was among the most significantly upregulated genes in E13.5 Actβcat dermis (Fig. 2B; Supplemental Table S1). Cell cycle scoring showed that Actβcat did not induce uniform cell cycle exit across the dermis; instead, cycling cells remained abundant, while *Cdkn1a*$^+$ Actβcat cells were shifted away from S phase (Supplemental Fig. S2C). Quantitative FISH confirmed elevated *Lef1* expression relative to controls and showed that Wnt target levels did not exceed those observed in wild-type DC cells, indicating that activated β-catenin increases Wnt signaling within the physiological range observed in wild-type DC cells (Fig. 2C; Supplemental Fig. S2D). Constitutive Wnt activation was sufficient to induce *Cdkn1a* (*p21*) expression at E13.5, and *Cdkn1a*$^+$ cells exhibited reduced EdU incorporation in contrast to neighboring *Cdkn1a*$^-$ cells (Fig. 2C).

By E14.5, DCs were present in both control and Actβcat embryos but were enlarged in mutants (Supplemental Fig. S2E). In controls, *Cdkn1a* expression was largely restricted to *Sox2*$^+$ DC cells, whereas in Actβcat mutants, it extended into surrounding *Sox2*$^-$ upper dermal cells (Fig. 2D). Both *Sox2*$^+$ and *Sox2*$^-$ cells expressing high *Cdkn1a* showed low EdU incorporation. Thus, enlarged Actβcat DCs are not explained by continued proliferation of *Sox2*$^+$ DC cells, but are more consistent with increased incorporation of Wnt-responsive dermal cells into *Cdkn1a*-positive and DC states. *Sox2*$^+$ cells in Actβcat mutants were closest to placodes and expressed the highest *Ptch1* levels, whereas surrounding mutant *Cdkn1a*$^+$*Sox2*$^-$ cells expressed lower *Ptch1* levels, indicating that DC gene expression remains associated with higher SHH pathway activity (Fig. 2E). Thus, elevated Wnt activity induces cell cycle exit in the absence of SHH ligand expression and without detectable DC marker induction. DC marker expression instead remains associated with SHH pathway activation, consistent with a requirement for SHH input during DC differentiation.

SHH pathway activation cell-autonomously elevates Wnt activity and promotes cell cycle exit

Our results show that elevated Wnt activity induces cell cycle exit without detectable DC markers. We next asked whether SHH activation could initiate DC gene expression without cell cycle exit. To test this, we expressed constitutively activated Smoothened (*Axin2CreER; RosaLSL-Smom2YFP*, referred to here as ActSMO) in the dermis prior to DC formation when Wnt signaling levels are low (Fig. 3A, tamoxifen E11.5). Whole-mount analysis of E14.5 skin showed that SHH activation in Wnt-active dermal cells induced large Sox2$^+$ dermal clusters in the upper dermis (Fig. 3B). These clusters formed autonomously without placodes, indicating that DC gene expression can occur without placode-derived Wnt ligands (Qu et al. 2022). Many peripheral Sox2$^+$ cells incorporated EdU, indicating that DC marker expression can occur without immediate cell cycle exit. In contrast, Sox2$^+$ cells in cluster centers lacked EdU incorporation, similar to quiescent DC cells in wild-type embryos.

Given the observed quiescent central Sox2$^+$ dermal cells (Fig. 3B), we examined whether ActSMO induced molecular changes similar to those observed in E13.5 Actβcat dermis. scRNA-seq analysis of E13.5 ActSMO and control dermis showed high *Ptch1* expression in recombined ActSMO cells (Fig. 3C). *Lef1* expression remained enriched in ActSMO upper dermal (UD) cells but was significantly elevated compared with controls. FISH confirmed increased *Lef1* expression in ActSMO dermis despite the absence of placodes (Fig. 3D). This elevated *Lef1* response was heterogeneous; cells with the highest *Lef1* levels were *Ptch1*-positive and tended to form aggregates with elevated *Cdkn1a* and reduced EdU incorporation, surrounded by cells with lower and more variable *Lef1* (Fig. 3D,E). Importantly, only *Ptch1*$^+$ (recombined) cells showed elevated *Lef1* expression, while neighboring *Ptch1*-negative cells (nonrecombined) retained normal *Lef1* levels, indicating a cell-autonomous effect. Together, these results show that SHH activation elevates Wnt signaling cell-autonomously and promotes cell cycle exit in Wnt-responsive cells, without placode-derived Wnt ligands.

GeneTrajectory resolves transcriptional programs associated with cell cycle exit

In the ActSMO condition, DC genes are expressed in proliferating cells (Fig. 3B), indicating that DC gene expression can occur without immediate cell cycle exit. To resolve the gene programs underlying these separable processes, we applied GeneTrajectory (GT), a computational approach that separates co-occurring gene programs from whole-transcriptome scRNA-seq data (Qu et al. 2024).

Applying GT to E14.5 wild-type dermal scRNA-seq data identified three gene trajectories, corresponding to proliferation (S/G2/M), DC differentiation and lower dermal differentiation (Supplemental Fig. S3A). The DC trajectory was partitioned into stages using gene bins and visualized by gene-bin scores. *Lef1* and *Ptch1* expression covaried across DC trajectory stages and peaked at the terminal stage 6 (Supplemental Fig. S3B). Canonical DC genes, including *Gal*, *Sox18*, and *Sox2*, were similarly enriched at stage 6 (Supplemental Fig. S3C). Stage 6 cells were largely quiescent with a G1 fraction near 1.0 and elevated *Cdkn1a* expression, indicating that cell cycle exit coincides with molecular DC differentiation at the trajectory terminus.

We next applied GT to E13.5 ActSMO dermal scRNA-seq data, where DC gene expression and cell cycle exit are tightly coupled in wild type. GT identified four trajectories (Fig. 4A; Supplemental Fig. S3D). Two corresponded to proliferation (S/G2/M) and lower dermal differentiation, whereas two additional trajectories were unique to ActSMO dermis. One contained DC genes and the second lacked DC markers (Fig. 4B; Supplemental Fig. S3D). Cells expressing this latter program localized to a subset of Wnt-active cells and were largely restricted to G1/G0 phase (Fig. 4B). Pathway analysis revealed enrichment for TP53-associated cell cycle inhibitory genes, including *Trp53inp1* and *Plk2*, overlapping with *Cdkn1a* expression (Fig. 4C; Supplemental Table S1). FISH confirmed significant upregulation of both *Cdkn1a* and *Trp53inp1* in the E13.5 ActSMO dermis relative to controls (Figs. 3D, 4D; Supplemental Fig. S3E).

Trp53inp1$^+$ ActSMO cells exhibited significantly higher *Lef1* levels than control upper dermal cells (Fig. 4D), consistent with SHH-dependent elevation of Wnt activity and cell cycle exit. To test whether elevated Wnt signaling alone induces this program, we applied GT to E13.5 Actβcat dermis, which induces *Cdkn1a* but not DC genes (Supplemental Fig. S3F). A similar *Trp53inp1*-containing trajectory was identified in Actβcat mutants (Supplemental Table S1). Module projection (label transfer) of the ActSMO trajectory onto Actβcat and control data sets revealed a shared molecular state in both mutants that was absent in controls (Fig. 4E).

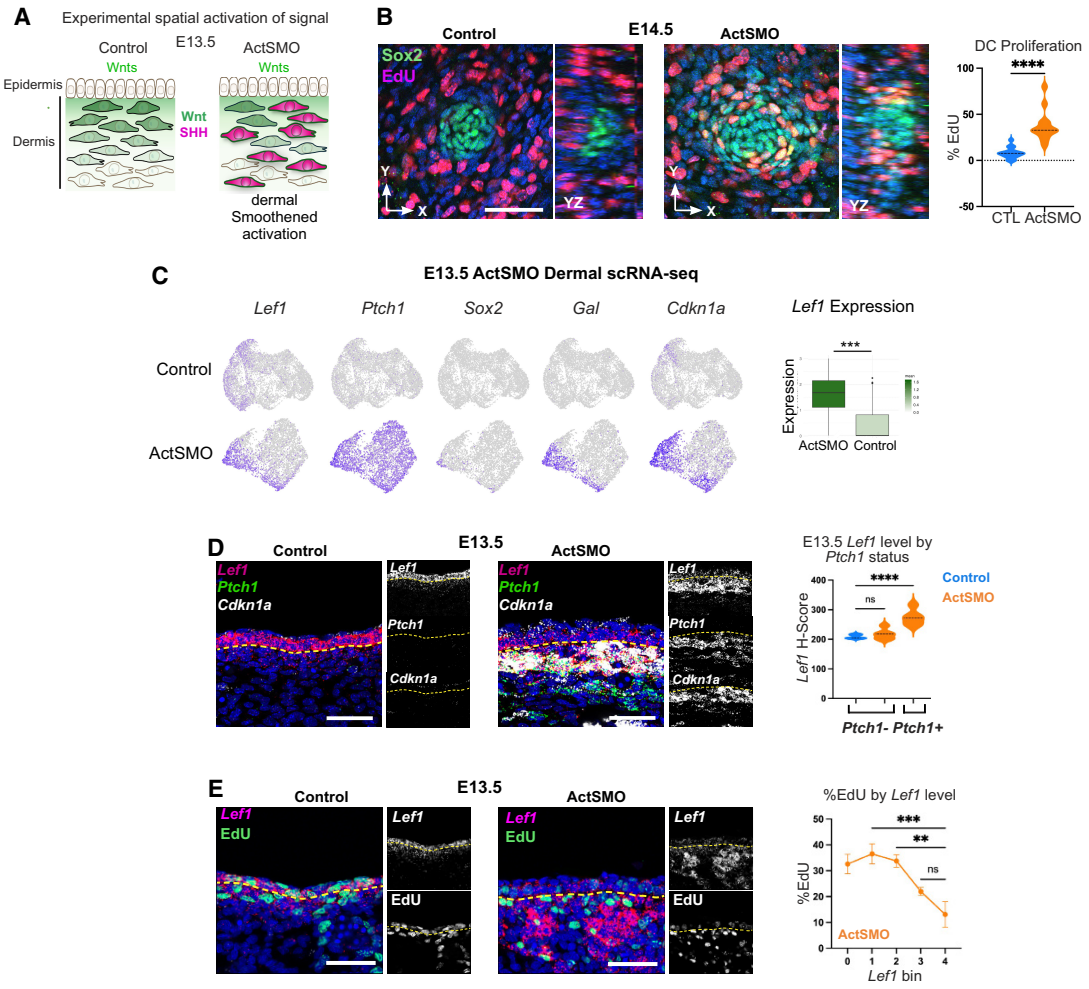


Figure 3. SHH pathway activation cell-autonomously elevates Wnt activity and promotes cell cycle exit. (*A*) Experimental design for constitutive dermal Smoothened activation before DC formation (tamoxifen at E11.5). (*B*) Whole-mount E14.5 control and ActSMO skin stained for Sox2 and EdU; quantification of the percentage of EdU$^+$ in Sox2$^+$ DC cells ($n = 8$). (*C*) E13.5 control and ActSMO dermal scRNA-seq UMAPs colored by indicated genes. (*Right*) *Lef1* expression in upper dermal cells. (*D*) E13.5 *Lef1*/*Ptch1*/*Cdkn1a* FISH and quantification of *Lef1* levels by *Ptch1* status ($n = 8$). (*E*) E13.5 *Lef1*/EdU FISH and quantification of EdU incorporation by *Lef1* bin in ActSMO dermis. Yellow dashed lines mark the epidermal–dermal boundary. Quantifications include six to eight follicles or regions per embryo from two to three embryos unless otherwise indicated. Data are mean ± SEM; one-way ANOVA. (ns) Not significant. Scale bars, 50 µm.

To determine whether this program reflects a general consequence of reduced proliferation, we analyzed E13.5 Wntless conditional knockout embryos (*K14Cre;Wls*$^{fl/fl}$) in which epidermal Wnt ligand secretion is disrupted and dermal proliferation is reduced (Chen et al. 2012; Fu and Hsu 2013; Qu et al. 2024). Label transfer of the ActSMO/Actβcat-specific trajectory was not detected in Wntless cKO dermis (Fig. 4E; Supplemental Fig. S3G). Notably, dermal proliferation is reduced in Wntless mutants despite the absence of this program, indicating that the exit trajectory reflects an elevated Wnt-dependent developmental transition rather than generic cell cycle arrest caused by reduced proliferation.

Finally, we examined cell cycle dynamics of cells expressing this program. At E13.5 and E14.5, most ActSMO *Trp53inp1*$^+$ cells showed low EdU incorporation comparable to quiescent DC cells (Fig. 4F; Supplemental Fig. S4A). EdU pulse chase experiments showed that many *Trp53inp1*$^+$ cells retained EdU similarly to wild-type DCs (Fig. 4F; Gupta et al. 2019; Qu et al. 2022). Although ActSMO dermal clusters contained proliferating *Sox2*$^+$ cells at E14.5, most became quiescent by E15.5 (Supplemental Fig. S4B), indicating that they exit the cell cycle after division. Together, these data define a shared gene program underlying cell cycle exit during the pre-DC-to-DC transition, which we term the exit gene trajectory.

Loss of GLI3 chromatin binding induces cell cycle exit downstream from elevated Wnt signaling

Although Wnt activity is required for dermal proliferation, our data indicate that elevated Wnt activity promotes cell cycle exit during DC formation (Chen et al. 2012; Gupta et al. 2019). To examine the mechanism, we profiled

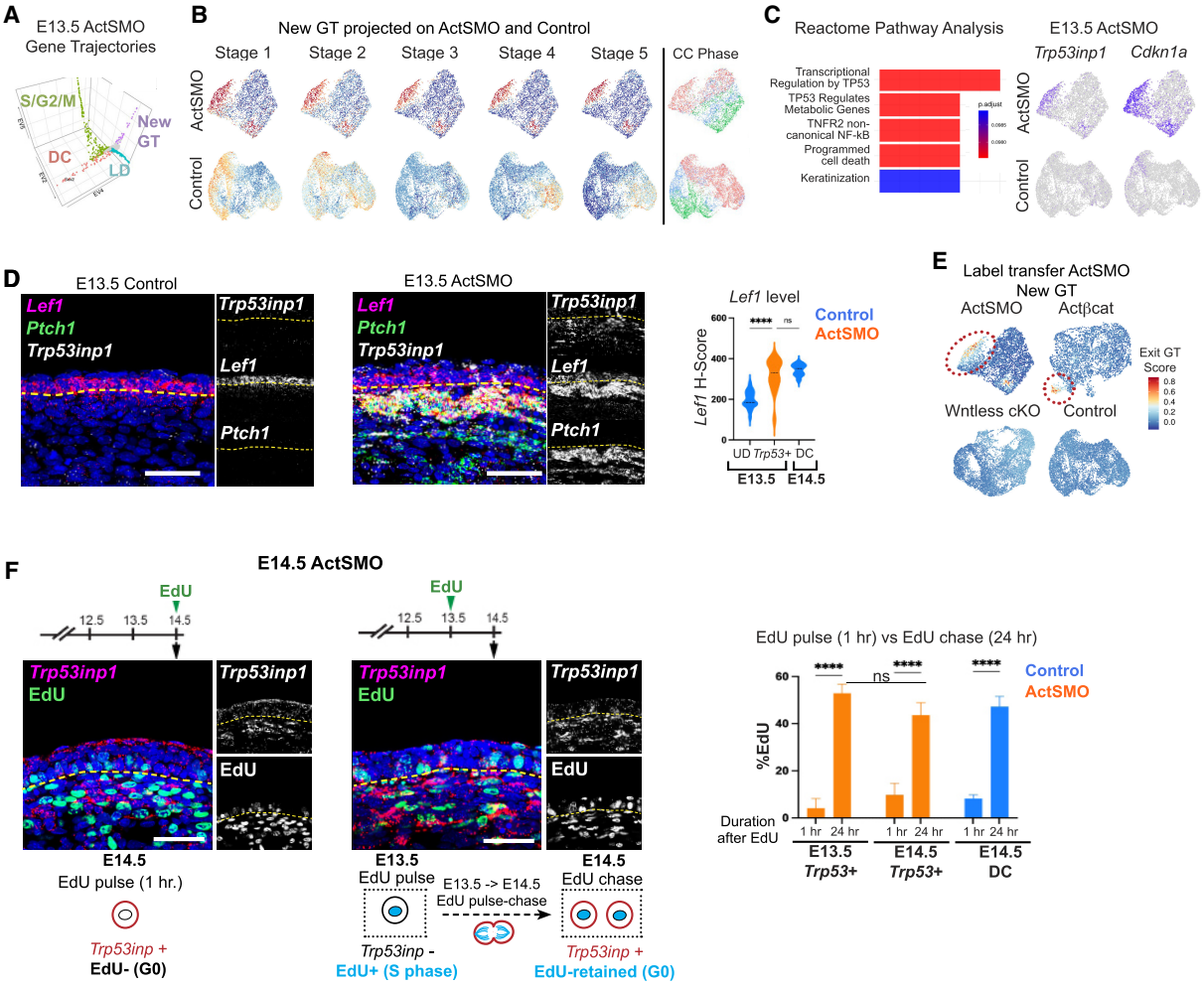


Figure 4. GeneTrajectory resolves transcriptional programs associated with cell cycle exit. (*A*) GeneTrajectory diffusion map of E13.5 ActSMO dermal cells. (*B*) Control and ActSMO dermal UMAPs colored by the ActSMO-specific new GT stage or cell cycle phase. (*C*) Reactome pathway analysis of new GT genes and UMAPs colored by indicated genes. (*D*) E13.5 control and ActSMO FISH for *Lef1*/*Ptch1*/*Trp53inp1*. (*Right*) Quantification of *Lef1* in the indicated cell populations ($n = 3$). (*E*) Label transfer of the ActSMO new GT onto indicated E13.5 data sets showing cells expressing the same gene module. (*F*) EdU pulse chase analysis of *Trp53inp1*$^+$ cells in ActSMO skin. EdU was given either 1 h before harvest at E14.5 or at E13.5 followed by a 24 h chase to E14.5; quantification shows EdU incorporation after 1 h pulse and retention after 24 h chase in *Trp53inp1*$^+$ cells ($n = 3$). The cartoon depicts recently divided cells becoming *Trp53inp1*$^+$ as they undergo cell cycle exit. Yellow dashed lines mark the epidermal–dermal boundary. Quantifications include six follicles or regions per embryo from two to three embryos unless otherwise indicated. Data are mean ± SEM; one-way ANOVA. (ns) Not significant. Scale bars, 50 µm.

CTNNB1/β-catenin binding in E13.5 Actβcat and control dermis. CTNNB1 binding was enriched at canonical Wnt targets (e.g., *Sp5*, *Axin2*, and *Lef1*) but not at *Cdkn1a*, exit GT genes, or other loci associated with cell cycle inhibition (Supplemental Fig. S5A). This raised the question of how elevated Wnt activity promotes exit without direct CTNNB1 binding at inhibitory genes. Because Wnt activity is elevated upon SHH activation, components of the SHH pathway could mediate Wnt-dependent exit. In other tissues, Wnt signaling regulates *Gli3* before SHH (Alvarez-Medina et al. 2008). Prior to SHH expression, GLI3 is predominantly present as a cleaved repressor that binds many SHH target loci (te Welscher et al. 2002; Vokes et al. 2008). FISH confirmed *Gli3* expression in Wnt-active dermal cells of control and Actβcat embryos at E13.5 before SHH ligand expression (Fig. 5A). To profile GLI3 binding, we performed CUT&RUN in E13.5 Actβcat and control dermis using *Gli3FLAG* embryos. GLI3 occupancy was globally reduced in Actβcat dermis, reflected by decreased reads at transcriptional start sites (Fig. 5B). De novo motif analysis confirmed enrichment of GLI motifs at regions with reduced binding (Supplemental Fig. S5B). These regions were enriched near genes associated with SHH signaling, although canonical SHH targets, including *Ptch1* and *Gli1*, were not expressed and lacked active histone marks at E13.5 (Fig. 5C,E; Supplemental Fig. S5C). Western blot confirmed that cleaved GLI3 protein levels were retained in the Actβcat mutant, indicating that reduced chromatin occupancy was not due to loss of GLI3 protein (Supplemental Fig. S5D). Thus, elevated Wnt signaling

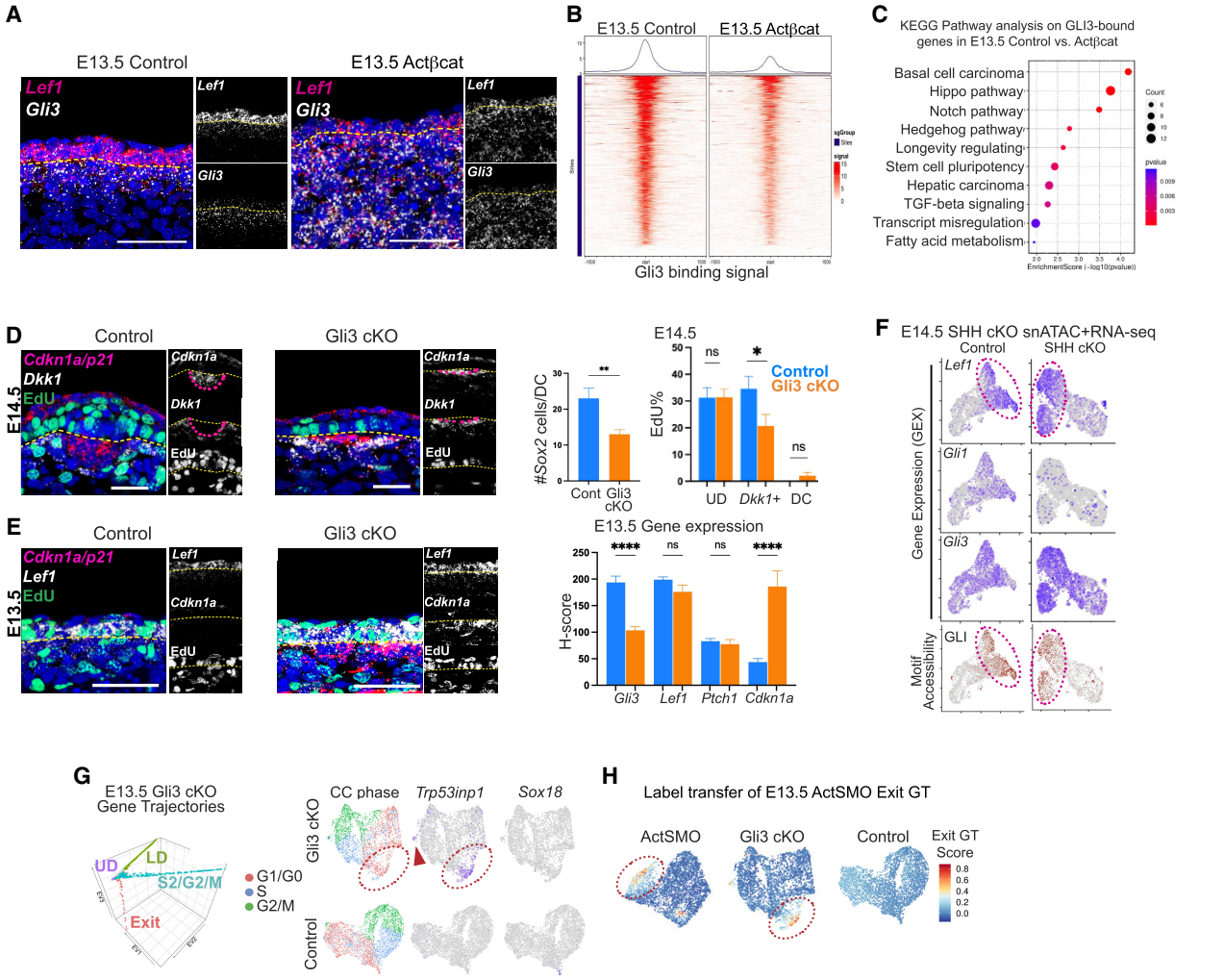


Figure 5. Loss of GLI3 chromatin binding induces cell cycle exit downstream from elevated Wnt signaling. (*A*) *Gli3* and *Lef1* expression in E13.5 control and Actβcat skin before DC formation. (*B*) Heat map of GLI3 binding at transcriptional start sites (TSS) in E13.5 control and Actβcat skin. (*C*) KEGG pathway analysis of GLI3 unbound regions in Actβcat. (*D*) E14.5 control and Gli3 cKO *Cdkn1a*/*Dkk1*/EdU FISH with quantification of *Sox2*$^+$ DC cells and the percentage of EdU by cell type ($n = 3$). (*E*) E13.5 control and Gli3 cKO *Cdkn1a*/*Lef1*/EdU FISH with quantification of the indicated genes ($n = 4$). (*F*) Integrated snATAC + RNA-seq UMAPs of E14.5 control and epidermal SHH cKO showing gene expression and GLI motif accessibility. (*G*) GeneTrajectory diffusion map and UMAPs of E13.5 control and Gli3 cKO dermal cells, identifying an exit GT. (*H*) Label transfer of ActSMO exit trajectory onto Gli3 cKO and control scRNA-seq data sets. Yellow dashed lines mark the epidermal–dermal boundary. Quantifications include six follicles or regions per embryo from two to three embryos unless otherwise indicated. Data are mean ± SEM; one-way ANOVA. (ns) Not significant. Scale bars, 50 µm.

reduces GLI3 chromatin binding before SHH ligand expression.

To test whether loss of GLI3 induces exit, we ablated *Gli3* in the dermis (*Axin2CreER;Gli3*$^{fl/fl}$, referred to here as Gli3 cKO). At E14.5, DCs in Gli3 cKO embryos were smaller than controls, and *Dkk1*$^+$ peri-DC cells showed premature *Cdkn1a* upregulation and reduced EdU incorporation (Fig. 5D; Supplemental Fig. S5E). Similarly, at E13.5 before DC formation, Gli3 cKO dermal cells exhibited increased *Cdkn1a* expression (Fig. 5E). These *Cdkn1a*$^+$ cells showed reduced proliferation, phenocopying Actβcat dermis (Supplemental Fig. S5F).

FISH confirmed reduced *Gli3* expression in E13.5 Gli3 cKO dermis, while Wnt target expression was unaffected, placing GLI3 downstream from Wnt activity (Fig. 5E; Supplemental Fig. S5G). Canonical SHH targets remained inactive, showing that loss of GLI3 does not broadly derepress SHH targets. To assess whether GLI3 binding is associated with chromatin organization, we performed Micro-C in E13.5 wild-type dermis. GLI3-bound loci were modestly enriched in open chromatin compartments but rarely formed chromatin loops and lacked active promoter marks (Supplemental Fig. S5H). In contrast, canonical Wnt targets (e.g., *Lef1* and *Sp5*) formed chromatin loops and showed active histone modifications. Moreover, snATAC + RNA-seq analysis of E14.5 embryos lacking epidermal *Shh* showed GLI motif accessibility localized to Wnt-active cells even without

GLI activator function (Fig. 5F). These results indicate that GLI3 binding marks regulatory regions before SHH activation but does not broadly repress target-gene transcription.

scRNA-seq analysis of E13.5 Gli3 cKO dermis showed reduced *Gli3* expression with retained Wnt target gene expression (Supplemental Fig. S6A,B). GT analysis identified four trajectories, including a trajectory absent in controls that overlapped with the exit GT identified in Actβcat and ActSMO mutants (Fig. 5G; Supplemental Fig. S6C). This trajectory was enriched for cell cycle inhibitory genes, including *Trp53inp1*. Label transfer of the ActSMO exit GT onto the Gli3 cKO data set identified a corresponding population expressing this gene program (Fig. 5H), indicating that this exit program is shared across ActSMO, Actβcat, and Gli3 cKO conditions.

EdU pulse chase experiments showed that *Cdkn1a*-high cells in Gli3 cKO dermis were quiescent but derived from recent cell divisions (Supplemental Fig. S5F). Cross-referencing genes that lost GLI3 binding in Actβcat dermis with genes upregulated in Gli3 cKO dermis identified multiple cell cycle inhibitory genes, including *Mxd4* and *Efna5* (Supplemental Fig. S6D). Exit GT genes, including *Baiap2* and *Cpt1c*, also showed reduced GLI3 binding and increased expression. Together, these data indicate that β-catenin and Gli3 act in a shared pathway regulating cell cycle exit: elevated Wnt signaling reduces GLI3 chromatin occupancy and induces cell cycle exit-associated genes without broadly activating canonical SHH target genes (Supplemental Fig. S6E).

Broad SHH pathway activation induces dermal condensate gene expression across the Wnt gradient

In contrast to wild-type embryos where DC genes are induced abruptly as cells exit the cell cycle, broad SHH pathway activation can induce DC gene expression without immediate cell cycle exit (Fig. 3B). Because SHH pathway activation both induces DC genes and cell-autonomously elevates Wnt activity, DC gene induction under high SHH could reflect SHH signaling, elevated Wnt activity, or both. We therefore asked whether Wnt signaling level influences how DC genes are induced during broad SHH pathway activation.

To address this, we analyzed the DC gene trajectory in the E13.5 ActSMO mutant, in which SHH activation occurs across dermal cells spanning a range of Wnt activity (Fig. 6A; Supplemental Fig. S7A). In the E14.5 wild-type DC gene trajectory, DC genes are induced primarily at the terminal stage, coinciding with the highest levels of *Lef1* and *Ptch1* expression (Supplemental Fig. S3A–C). In contrast, in the ActSMO condition, DC genes (e.g., *Gal*, *Sox18*, and *Sox2*) were induced progressively across DC trajectory stages, with DC gene expression increasing with *Lef1* levels (Fig. 6B,C). Cells with the highest *Lef1* levels showed the greatest progression along the trajectory and the highest DC gene expression. Notably, early stages retained a high proliferative fraction, whereas terminal-stage cells were largely quiescent (G1/G0 fraction ~0.9). Similarly, ActSMO cells expressing lower levels of the DC marker *Gal* showed high EdU incorporation, whereas

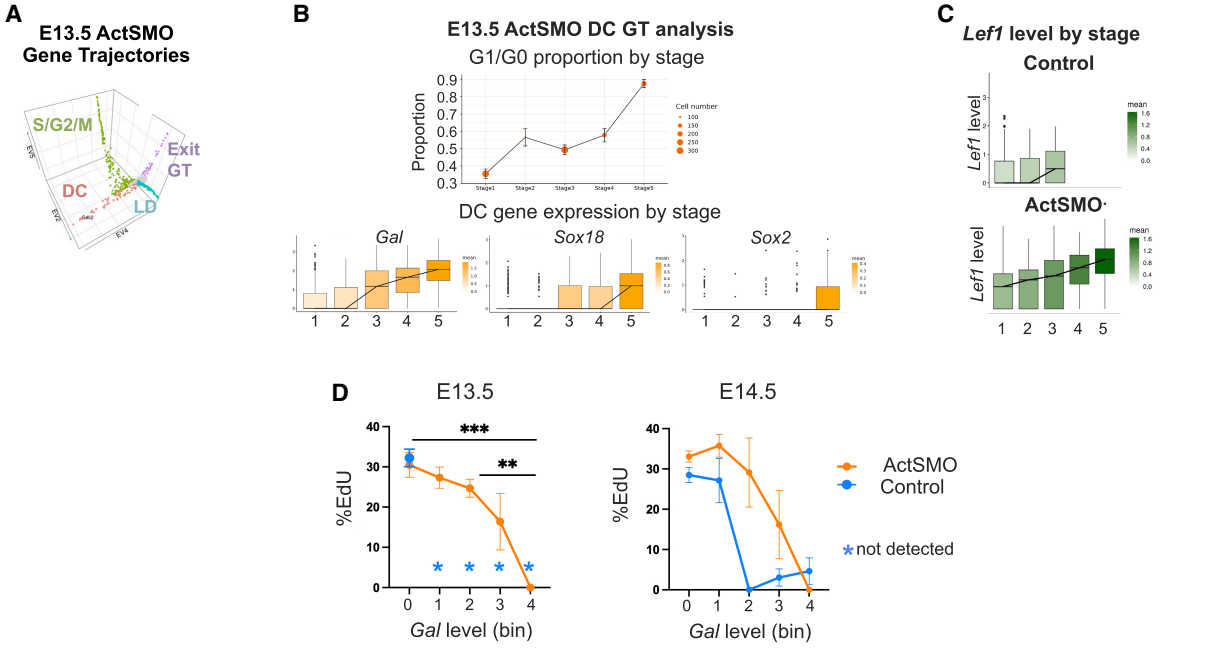


Figure 6. Broad SHH pathway activation induces dermal condensate gene expression across the Wnt gradient. (*A*) GeneTrajectory diffusion map of E13.5 ActSMO dermal cells. (*B*) G1/G0 fraction and expression of indicated DC genes by DC trajectory stage. (*C*) *Lef1* levels by trajectory stage in control and ActSMO dermis. (*D*) E13.5 and E14.5 EdU incorporation by *Gal* level in control and ActSMO dermis (blue asterisks indicate *Gal* bins not detected in control); $n = 3$ embryos. Data are mean ± SEM; one-way ANOVA. (ns) Not significant.

Gal-high cells were largely nonproliferative like wild-type DC cells (Fig. 6D; Supplemental Fig. S7B). Together with the EdU pulse chase results showing that these cells subsequently become quiescent (Fig. 4F; Supplemental Fig. S4B), these findings indicate that broad SHH pathway activation expands DC-associated intermediate states in which DC gene induction precedes cell cycle exit.

Consistent with the requirement for Wnt signaling in DC differentiation, cells with high SHH activity but lacking Wnt activity in the ActSMO condition show minimal or undetectable DC gene expression (Fig. 3C; Qu et al. 2022). Thus, broad SHH activation expands the window over which Wnt-responsive cells initiate DC gene expression, resulting in progressive rather than abrupt induction of DC genes. Together with the Actβcat analysis, these data indicate that DC gene expression is highest where elevated Wnt activity coincides with SHH pathway activity (Fig. 6C).

Coordinated Wnt and SHH activity aligns cell cycle exit with DC differentiation

Because exit and DC differentiation coincide where high Wnt activity overlaps with SHH signaling, we tested whether coactivation of these pathways is sufficient to coordinate cell cycle exit with DC differentiation. In wild-type skin, this overlap occurs in dermal cells adjacent to placodes. We therefore induced epidermal SHH expression at E13.5 (*K14Cre;Rosa-LSL-SHH*, referred to here as SHH OE) to activate SHH signaling in Wnt-active dermal cells before placode formation (Fig. 7A; Reddy et al. 2001; Phan et al. 2020). FISH analysis showed that *Lef1* and *Ptch1* covaried with dermal depth with highest levels in the most superficial dermis (Fig. 7B). *Lef1* levels were increased relative to E13.5 controls, indicating that SHH elevates Wnt activity. DC genes (e.g., *Sox2* and *Gal*) were restricted to superficial layers and coincided with *Cdkn1a* expression and low EdU incorporation (Fig. 7C; Supplemental Fig. S8A). *Dkk1* localized to a deeper dermal layer beneath DC gene-expressing cells. scRNA-seq analysis of E13.5 SHH OE dermis confirmed overlapping *Lef1* and *Ptch1* expression, with DC genes and *Cdkn1a* restricted to cells with the highest combined signal levels (Supplemental Fig. S8C).

GT analysis identified three trajectories corresponding to proliferation, lower dermal differentiation and DC differentiation, similar to E14.5 wild-type dermis (Fig. 7D; Supplemental Fig. S8B). Unlike the ActSMO and Actβcat conditions, a distinct exit trajectory was not detected. Within the DC trajectory, *Lef1* and *Ptch1* increased coordinately, and DC genes and *Cdkn1a* were induced synchronously at the terminal stage, coincident with quiescence (Fig. 7D; Supplemental Fig. S8C). Thus, when Wnt and SHH activities covary, DC differentiation and cell cycle exit are aligned within a single DC trajectory.

We next examined whether GLI3 chromatin occupancy is similarly reduced when Wnt and SHH signaling are coactivated. GLI3 CUT&RUN analysis in SHH OE dermis showed global depletion of GLI3 binding (Fig. 7E), indicating that GLI3 displacement is not an artifact of genetic stabilization of β-catenin. Loss of GLI3 binding occurred at cell cycle regulatory genes (*Mxd4* and *Efna5*) associated with active histone marks (Supplemental Fig. S8D). In contrast to Actβcat mutants, SHH target genes (*Ptch1* and *Gli1*) were transcriptionally activated, accompanied by increased H3K4me3 and H3K27ac signal (Fig. 7E). Because SHH signaling converts cleaved GLI3 repressor into full-length GLI activator, the observed loss of GLI3 occupancy likely reflects replacement by other GLI activators at SHH target loci (Supplemental Fig. S8E). These data indicate that Wnt and SHH coactivation removes GLI3 from exit-associated genes, while activating canonical SHH target genes.

To test whether varying Wnt and SHH inputs are sufficient to coordinate these processes outside of the tissue context, we reconstituted the system in vitro by using E13.5 PDGFRαH2BGFP dermal cells (Hamilton et al. 2003). These cells showed dose-dependent gene responses to the Wnt agonist (CHIR99021) or the Smoothened agonist (SAG) (Supplemental Fig. S9A). SAG enhanced *Lef1* expression in CHIR-treated cells (Supplemental Fig. S9B). High CHIR alone induced *Cdkn1a*, whereas combined CHIR and SAG treatment induced DC genes, including *Gal* and *Sox18*.

To assess morphogenesis, E13.5 dermal cells were seeded onto a collagen-based 3D matrix with varying CHIR and SAG concentrations (Fig. 7F; Supplemental Fig. S9C). High CHIR (5 µM) with 50 nM SAG produced large dermal clusters with low proliferation that expressed Robo2, a DC gene that regulates cell migration (Goncalves et al. 2020; Guzmán-Palma et al. 2021). Clusters from other conditions did not express Robo2 and contained more $Ki67^+$ cells. Thus, coupled Wnt and SHH activity is sufficient to induce molecular differentiation with concurrent low proliferation in vitro.

Together, these results indicate that the pre-DC-to-DC transition comprises separable events, DC gene induction and cell cycle exit, that are normally coordinated by Wnt and SHH activity. We propose that localized SHH elevates Wnt response in the same cells in which it induces DC genes, aligning DC gene induction with cell cycle exit within a narrow transition window. This coordination compresses, rather than eliminates, intermediate states: they are transient, spatially confined, and few in number, producing a sharp DC boundary. In contrast, broad SHH pathway activation in ActSMO induces DC gene expression across a wider field and a range of Wnt response levels. Across this trajectory, Wnt activity, DC gene expression, and cell cycle exit covary (Fig. 6B–D); cells with lower Wnt activity express DC genes at lower levels and remain proliferative, increasing the abundance and distribution of intermediate states and producing an expanded boundary (Fig. 7G).

Discussion

In this study, we identify a mechanism by which interacting morphogen signals generate sharp cell type boundaries

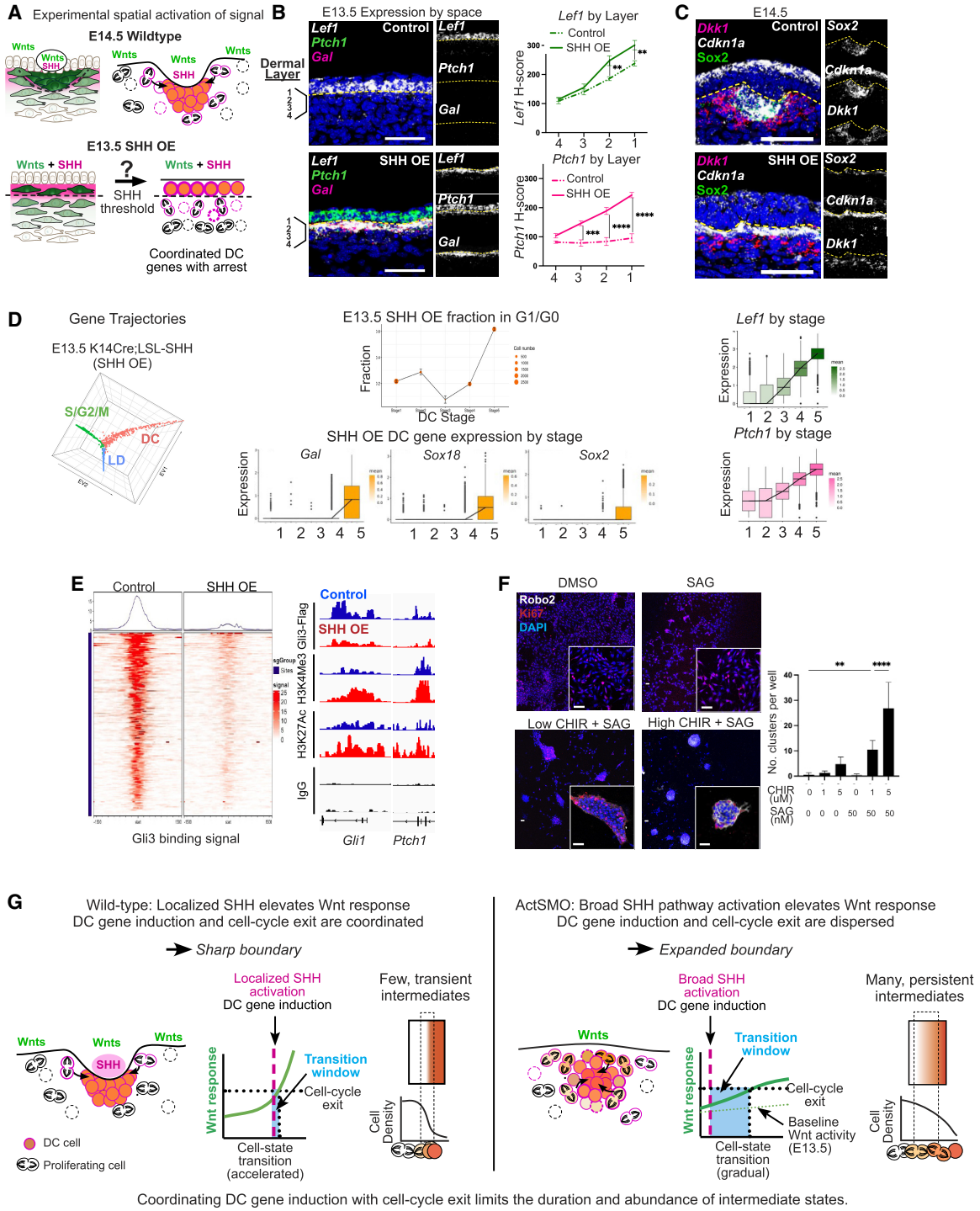


Figure 7. Coordinated Wnt and SHH activity aligns cell cycle exit with DC differentiation. (*A*) Experimental design for epidermal Wnt and SHH ligand coexpression at E13.5 (SHH OE). (*B*) E13.5 control and SHH OE FISH, showing increased *Ptch1* and *Lef1* levels across upper dermal layers ($n = 3$). (*C*) E14.5 control and SHH OE FISH showing *Cdkn1a*/*Dkk1*/*Sox2* expression ($n = 3$). (*D*) GeneTrajectory diffusion map of E13.5 SHH OE dermal cells, G1/G0 fraction, DC gene expression, and *Lef1* and *Ptch1* levels by DC GT stage. (*E*) Heat map of GLI3 binding at TSS in E13.5 control and SHH OE skin with genome browser tracks at *Gli1* and *Ptch1*. (*F*) Three-dimensional dermal cultures stained for Robo2 and Ki67 with quantification of dermal clusters. (*G*) Model: localized SHH aligns DC gene induction with Wnt-associated cell cycle exit, limiting the duration and abundance of intermediate states and producing a sharp boundary. The blue region denotes the transition window between DC gene induction and cell cycle exit along the DC state transition. In wild type, this window is narrow, whereas broad cell-autonomous SHH pathway activation in ActSMO expands this window and intermediate-state occupancy, producing an expanded boundary. Yellow dashed lines mark the epidermal–dermal boundary. Quantifications include six to eight follicles or regions per embryo from two to three embryos unless otherwise indicated. Data are mean ± SEM; one-way ANOVA. (ns) Not significant. Scale bars, 50 µm.

by coordinating separable cellular events of a cell-state transition. During dermal condensate (DC) formation, we show that Sonic Hedgehog (SHH) acts on Wnt-responsive cells to elevate Wnt activity, while also promoting DC gene induction. Elevated Wnt activity promotes cell cycle exit through reduced chromatin binding of the transcriptional repressor GLI3. Thus, Wnt and SHH have distinguishable effects under perturbation, but are normally integrated to align DC gene induction with cell cycle exit. This coordination limits the duration and abundance of intermediate states, causing transitional cells to remain sparse and spatially confined. Here, boundary sharpness reflects compression of a developmental transition, rather than absence of intermediate states. Although our data show that Wnt and SHH coordinate DC gene induction with cell cycle exit, they do not determine how cell movement, aggregation, and mixing contribute to the final DC boundary. EdU pulse chase experiments show that labeled cells can incorporate into the DC rather than remaining fixed at the periphery, suggesting that cell rearrangement likely helps refine the boundary.

Classical morphogen-based models explain sharp boundaries through concentration thresholds that specify distinct cell states, as shown for SHH in the vertebrate neural tube and for BMP along the dorsoventral axis (Roelink et al. 1995; Greenfeld et al. 2021; Benzinger and Briscoe 2025). Our findings suggest an additional principle for systems where neighboring cell types are connected by a continuous transition. In these systems, boundary sharpness also depends on the abundance of intermediate states. Intermediate cells accumulate when they continue to proliferate, whereas coordinating cell cycle exit with differentiation limits their expansion and allows the transition to resolve with few intermediates. Thus, morphogen thresholds may determine where a transition occurs, while regulation of intermediate-state accumulation determines how sharply it is resolved. Notably, ActSMO clusters do not support placode formation despite their large size, whereas compact DCs, including those in Actβcat skin, support hair follicle formation. This suggests that DC organization, rather than size alone, may be important for productive epithelial–mesenchymal signaling. Future studies will be needed to determine whether and how DC compactness contributes to placode formation and subsequent follicle growth.

Although tight coupling of Wnt and SHH activities produces a sharp transition during DC formation, variation in the timing, strength, or spatial alignment of interacting morphogen gradients may support alternative modes of tissue organization. In systems containing transit-amplifying populations, differentiation can proceed without immediate cell cycle exit, expanding intermediate states and producing graded boundaries (Morita et al. 2021; Sun et al. 2023). Thus, the duration and abundance of transitional states are tunable outputs of morphogen coordination that regulate boundary sharpness across tissues (Fig. 7G). Additional pathways, including FGF signaling, have been implicated in DC formation and may act upstream of SHH in this process (Biggs et al. 2018; Mok et al. 2019; Qu et al. 2022). Broadly, these findings suggest that precise tissue organization in regenerative and engineered systems depends not only on establishing cell identity, but on controlling the duration and abundance of intermediate states during developmental transitions.

How SHH signaling elevates Wnt activity is unlikely to involve direct transcriptional activation of Wnt target genes by GLI factors. Instead, elevated Wnt activity is associated with loss of GLI3 chromatin occupancy at loci involved in cell cycle regulation. Although GLI3 eviction does not produce large-scale chromatin reorganization, it coincides with SHH-dependent activation of differentiation genes, suggesting that chromatin-level cross-regulation between Wnt and SHH pathways aligns exit with differentiation.

At the tissue level, this SHH-dependent enhancement of Wnt responsiveness shapes how the developmental transition unfolds across space and cell state. Prior to SHH signaling, dermal cells occupy a range of states along a Wnt-defined continuum that reflects differences in transcriptional state. Rather than prespecifying DC fate, these differences influence how cells respond once SHH is present. Cells with higher Wnt activity are associated with greater DC gene induction and reduced EdU incorporation, whereas lower-Wnt states retain more proliferative intermediate cells. Thus, SHH acts on a prepatterned field of cells, coordinating DC gene induction with cell cycle exit locally to compress the developmental transition and limit the accumulation of intermediate states. In this view, pre-existing differences in cell state influence how cells respond to inductive signals instead of assigning fate in advance, distinguishing this mechanism from strict threshold-based positional specification or self-organization from an initially uniform field.

This work establishes an experimentally tractable mammalian system for investigating how interacting morphogen gradients regulate the timing of concurrent biological processes. Integrating in vivo genetics with single-cell trajectory analysis resolves overlapping differentiation programs that are otherwise difficult to detect due to their limited duration and abundance, revealing how dynamic signaling interactions shape discrete cell-state transitions (Qu et al. 2024).

Materials and methods

Mouse strains and tamoxifen induction

Embryos were staged as days after coitum by vaginal plug detection. Pregnant dams received a single tamoxifen dose (20 mg/mL in corn oil; 30–60 μg/g body weight; Sigma) by gavage at E11.5. Axin2CreER (van Amerongen et al. 2012) mice were crossed with Rosa-LSLSmoM2YFP (Jeong et al. 2004), β-catenin$^{fl(Ex3/+)}$ (Harada et al. 1999) and *Gli3*$^{fl/fl}$ (Blaess et al. 2008) mice. K14Cre (Dassule et al. 2000) mice were bred to Shh overexpressor (Wang et al. 2010) and *Wntless*$^{fl/fl}$ (Carpenter et al. 2010) mice. *Rosa-FLAG-Gli3YFP* (Vokes et al. 2008) mice were crossed with Axin2CreER and β-catenin$^{fl(Ex3/+)}$ mice. R26Fucci2aR (Abe et al. 2013) mice were used to visualize cell

cycle phase. *PDGFRaH2BGFP* (Hamilton et al. 2003) mice were used for dermal cultures. A random population of both male and female mice was used. All procedures involving animal subjects were performed under the approval of the Institutional Animal Care and Use Committee of the Yale School of Medicine.

EdU incorporation assay

EdU (25 µg/g) was administered to pregnant mice intraperitoneally, and embryos were harvested after the indicated hours. EdU was detected using the Click-it EdU imaging kit (Alexa 555 or Alexa 488; Life technologies) following the manufacturer's instructions.

Whole-mount immunofluorescence

Dorsolateral skin was microdissected, placed on nucleopore filters (VWR) and fixed with 4% PFA. Explants were blocked and incubated overnight with anti-Sox2 (1:400; Abcam), anti-GFP (1:500; Abcam), and anti-RFP (1:500; Rockland) antibodies. Explants were washed and incubated overnight with Alexa Fluor 488 or 568 antirabbit or antichicken (1:200; Invitrogen) antibodies. Explants were washed and nuclear counterstained (Hoechst) before mounting onto slides.

Fluorescent in situ hybridization

Embryos were fixed in 10% formalin, paraffin-embedded, and sectioned. RNA FISH was performed using the RNAscope multiplex fluorescent detection kit (ACDBio) according to the manufacturer's instructions. Probe detection was done using HRP-C1-3 reagents and tyramide signal amplification (VIVID 650 and 570). EdU staining was done as described above. Probes used were Mm-Lef1 (441861), Mm-Ptch1 (402811), Mm-Dkk1 (402521), Mm-Sox2 (401041), Mm-Gal (400961), Mm-Gli3 (445511), and Mm-Trp53inp1 (1161531).

Microscopy

FISH images were acquired using the Leica Stellaris 8 DMi8 confocal microscope with a 40× oil immersion objective lens, scanned at 5 µm thickness and 1024 × 1024-pixel width. Skin explants were imaged using the LaVision TriM Scope II (LaVision Biotec) microscope equipped with a Chameleon Vision II (Coherent) two-photon laser (810–1000 nm) for 3D images ranging from 50 to 120 µm (2 µm serial optical sections) using a 20× water immersion lens (Olympus) and scanned with a field of view of 0.3–0.5 mm^2 at 800 Hz.

Single-cell dissociation

Embryonic dorsolateral skin was microdissected and pooled after genotyping (two to three embryos per condition) and dissociated into a single-cell suspension in 0.25% trypsin (Life Technologies) for 15 min at 37°C. DAPI-excluded live skin cells were FACS sorted and submitted for 10X Genomics library preparation at 1.0×10^6/mL or processed for CUT&RUN or micro-C experiments.

Single-cell RNA sequencing

Single-cell libraries were generated using the 10X Chromium single-cell 3′ v2 platform and sequenced on an Illumina NovaSeq 6000. Raw reads were processed using the Cell Ranger pipeline and aligned to the mm10 genome to generate gene-cell count matrices. Downstream analysis was performed in Seurat (Hao et al. 2021). Cells with >1000 detected genes, <25% mitochondrial content, and >5% ribosomal content were retained, and doublets were removed using scDblFinder. Data were log-normalized, and principal component analysis was performed on the top variable genes. UMAP was used for visualization and clustering was performed using Seurat FindClusters (resolution 0.5). Clusters expressing *Col1a1* were classified as dermal, and clusters expressing upper dermal markers, including *Lef1* and *Dkk1*, were used to define the upper dermal population.

GeneTrajectory inference

GeneTrajectory analysis was performed as described (Qu et al. 2024). For each data set, highly variable genes were identified using Seurat FindVariableFeatures. Genes expressed in >1% and <50% of cells were retained, and the top 2000 highly variable genes were used for trajectory inference. Highly variable genes were used to construct diffusion maps based on the top 20 PCs. Cell k-nearest neighbor graphs ($k = 10$) were generated from the top 10 diffusion components. Gene–gene Wasserstein distances were then calculated from the cell graph and used to construct a gene diffusion map. Gene trajectories and time steps were determined by inspection of gene embeddings. Trajectories were extracted sequentially from the gene diffusion map. At each iteration, the gene farthest from the origin among unassigned genes was selected as the trajectory terminus, and a random-walk procedure was used to identify genes belonging to that trajectory. This process was repeated until the remaining unassigned genes formed an indistinct central cloud without resolvable branch structure. For each trajectory, the diffusion time step was selected to recover the longest trajectory without incorporating this central cloud. Gene ordering along each trajectory was determined by the first nontrivial eigenvector of a recomputed diffusion map on the trajectory-specific Wasserstein distance submatrix.

Each trajectory was partitioned into five to six gene bins, and cells were assigned to stages based on expression of ≥50% of genes in the corresponding bin. For each cell, gene-bin scores were calculated from the average expression of genes in each bin, and the stage with the highest bin score was assigned as the dominant trajectory stage. Exit gene trajectory scores were calculated using Seurat AddModuleScore based on genes identified in the E13.5 ActSMO data set. Pathway enrichment analysis was performed using ReactomePA (Yu and He 2016), and cell cycle phase was estimated using Seurat cell cycle scoring

(Nestorowa et al. 2016). For comparative analysis, upper dermal cells from paired conditions were merged and analyzed using standard Seurat workflows. Differential abundance was assessed using DA-seq (Zhao et al. 2021), and differential gene expression was performed using Seurat FindMarkers.

Data set-specific trajectory numbers and diffusion time steps were as follows: E14.5 wild-type dermis: three trajectories ($t = 13$, $t = 10$, and $t = 5$); E13.5 ActSMO dermis: four trajectories ($t = 1$, $t = 3$, $t = 2$, and $t = 1$), with paired control: three trajectories ($t = 3$, $t = 2$, and $t = 2$); E13.5 SHH OE dermis: three trajectories ($t = 6$, $t = 3$, and $t = 3$), with paired control: three trajectories ($t = 5$, $t = 3$, and $t = 3$); E13.5 Actβ-cat dermis: four trajectories ($t = 3$, $t = 3$, $t = 2$, $t = 2$), with paired control: three trajectories ($t = 1$, $t = 3$, and $t = 3$); and E13.5 Gli3 cKO dermis: four trajectories ($t = 8$, $t = 7$, $t = 6$, and $t = 1$), with paired control: three trajectories ($t = 4$, $t = 3$, and $t = 1$).

Integrated snATAC + RNA-seq multiomic analysis

snRNA-seq and snATAC-seq data from E14.5 *K14Cre; Shh*$^{fl/fl}$ and control skin were processed using Seurat and Signac. RNA data were normalized using SCTransform, and ATAC data were reduced using latent semantic indexing (LSI). Modalities were integrated using weighted nearest neighbor (WNN) analysis, and joint UMAP embeddings were generated for visualization. Transcription factor motif accessibility was calculated using chromVAR.

CUT&RUN experiments

CUT&RUN was done using the CUTANA ChIC/CUT&RUN kit (EpiCypher) following the manufacturer's protocol. Approximately 5×10^5 cells were used for nuclei isolation and immobilization on ConA beads. Nuclei were incubated with primary antibodies (0.5 µg/reaction): IgG, H3K27ac, H3K4me3, FLAG, and CTNNB1. Libraries were prepared using the CUTANA library preparation kit and sequenced on an Illumina NovaSeq 6000. Reads were quality-filtered, trimmed, and aligned to the mm10 genome using Bowtie2. BAM files were processed using SAMtools, and peaks were called with MACS2 using IgG as control. Coverage tracks were generated using deepTools and visualized in IGV. Differential binding analysis was performed using DESeq2. Heat maps were generated using DiffBind and motif enrichment analysis was performed using HOMER.

Micro-C experiments

Micro-C was performed using the Dovetail Micro-C kit (Cantata Bio) following the manufacturer's protocol. E13.5 dissociated skin cells were crosslinked with formaldehyde. Chromatin was digested with micrococcal nuclease, proximity-ligated, reverse crosslinked, and purified. Libraries were prepared using the Dovetail library module and sequenced to 300 million reads per biological replicate. Reads were aligned to the mm10 genome using BWA-MEM. Valid ligation pairs were identified and filtered using the Pairtools pipeline. Contact matrices were generated at 5 kb resolution using cooler and normalized by iterative correction.

Chromatin loops were identified using Mustache and loop anchors intersected with CUT&RUN peaks using Bedtools. A/B compartments were calculated at 40 kb resolution using FAN-C. Interaction maps and compartment tracks were visualized using FAN-C.

Western blot

Cells were lysed in RIPA buffer, and proteins from clarified lysates were resolved on SDS-PAGE gels and transferred to PVDF membranes. Membranes were blocked in 5% BSA/TBST, incubated with primary antibodies (anti-FLAG and anti-Actin) overnight at 4°C, washed, and incubated with HRP-conjugated secondary antibodies. Proteins were detected by chemiluminescence.

Dermal cultures

E13.5 PDGFRαH2BGFP dermal cells were FACS-isolated. GFP$^+$ cells were cultured in DMEM with 10% FBS, penicillin–streptomycin, and L-glutamine and plated at 3×10^6 cells per well in 6 well plates. For chemical perturbation assays, cells were treated with CHIR99021 or SAG as indicated for 48–72 h. For 3D cultures, 3×10^5 cells were seeded in µ-slide 8 well glass-bottom chambers (Ibidi) precoated with 1.5 mg/mL polymerized collagen type I (Corning) before seeding. Cultures were fixed in 4% PFA; blocked in 5% normal donkey serum, 1% BSA, and 0.2% Triton X-100; and incubated overnight at 4°C with rat anti-Ki67 (Invitrogen) and rabbit anti-Robo2 (Cell Signaling), followed by Alexa Fluor-conjugated secondary antibodies (Invitrogen) and nuclear counterstain before imaging by confocal microscopy.

Quantitative PCR

RNA was isolated using the RNeasy mini kit (Qiagen) and reverse-transcribed using SuperScript III (Invitrogen). QPCR was performed using SYBR Green master mix (Thermo Fisher) on a Viia7 real-time PCR system. Reactions were run in technical triplicates and normalized to *Gapdh*. Relative expression was calculated using the $\Delta\Delta Ct$ method.

Image analysis and quantification

Images were analyzed using ImageJ and Adobe Photoshop. scRNA-seq visualizations were generated using ggplot2 in R. DC cell counts were quantified from 3D whole-mount mosaics (1000×1000 µm FOV; 60–100 µm depth); $n = 3$–4 embryos. Sox2$^+$, EdU$^+$ cells and RFP$^+$ cells were manually counted in ImageJ using orthogonal views. Upper dermis was defined as 10–20 µm below the epidermis. Peri-DC was defined as cells within two cell layers of Sox2$^+$ DCs. For RNA FISH, cells with four to five dots were considered

positive and expression levels were quantified by H-score based on weighted dot counts per cell.

Statistical analysis

All statistical values are expressed as mean ± SEM. Two-group comparisons used unpaired Student's *t*-test; multiple comparisons used one-way ANOVA with Tukey's test: $P < 0.05$ (*), $P < 0.01$ (**), $P < 0.001$ (***), and $P < 0.0001$ (****).

Data availability

All genomic data generated in this study have been deposited in the NCBI Gene Expression Omnibus (GEO): scRNA-seq (GSE342133), snRNA-seq/snATAC-seq multiome (GSE342281), CUT&RUN (GSE342896), and Micro-C (GSE342793). Previously published scRNA-seq data are available under GSE255534 and GSE280825.

Competing interest statement

The authors declare no competing interests.

Acknowledgments

We thank Radhika Atit, Mayumi Ito, Leonard Milstone, and Jonathan Levinsohn for their thoughtful feedback and discussion throughout this project. This work was supported by National Institutes of Health grants (R01AR076420 to P.M., and U54AG076043 and U54AG079759 to Y.K.) and the LEO Foundation (LF-OC-23-001347 to P.M.).

Author contributions: Conceptualization—P.M., Y.K., R.L., Y.J., and S.P. Methodology—P.M., R.L., Y.K., Y.J., S.P., E.-L.R.B., S.V., H.L., and J.Z. Software—R.L. and Y.K. Resources—M.M.T., K.A.P., and D.H.W. Investigation—P.M., R.L., Y.J., S.P., H.L., E.-L.R.B., and S.V. Writing—original draft—P.M. Writing—review and editing—P.M., R.L., Y.J., S.P., T.X., R.D., Y.K., C.H.L., S.L., and J.Z. Supervision—P.M. and Y.K. Funding acquisition—P.M.

References

Abe T, Sakaue-Sawano A, Kiyonari H, Shioi G, Inoue K, Horiuchi T, Nakao K, Miyawaki A, Aizawa S, Fujimori T. 2013. Visualization of cell cycle in mouse embryos with Fucci2 reporter directed by *Rosa26* promoter. *Development* **140:** 237–246. doi:10.1242/dev.084111

Alvarez-Medina R, Cayuso J, Okubo T, Takada S, Martí E. 2008. Wnt canonical pathway restricts graded Shh/Gli patterning activity through the regulation of Gli3 expression. *Development* **135:** 237–247. doi:10.1242/dev.012054

Benzinger D, Briscoe J. 2025. Investigating morphogen and patterning dynamics with optogenetic control of morphogen production. *Dev Cell* **60:** 3421–3430.e6. doi:10.1016/j.devcel.2025.07.019

Biggs LC, Mäkelä OJ, Myllymäki SM, Das Roy R, Närhi K, Pispa J, Mustonen T, Mikkola ML. 2018. Hair follicle dermal condensation forms via Fgf20 primed cell cycle exit, cell motility, and aggregation. *eLife* **7:** e36468. doi:10.7554/eLife.36468

Blaess S, Stephen D, Joyner AL. 2008. Gli3 coordinates three-dimensional patterning and growth of the tectum and cerebellum by integrating Shh and Fgf8 signaling. *Development* **135:** 2093–2103. doi:10.1242/dev.015990

Carpenter AC, Rao S, Wells JM, Campbell K, Lang RA. 2010. Generation of mice with a conditional null allele for *Wntless*. *Genesis* **48:** 554–558. doi:10.1002/dvg.20651

Chase HB, Rauch R, Smith VW. 1951. Critical stages of hair development and pigmentation in the mouse. *Physiol Zool* **24:** 1–8. doi:10.1086/physzool.24.1.30152098

Chen D, Jarrell A, Guo C, Lang R, Atit R. 2012. Dermal β-catenin activity in response to epidermal Wnt ligands is required for fibroblast proliferation and hair follicle initiation. *Development* **139:** 1522–1533. doi:10.1242/dev.076463

Chiang C, Swan RZ, Grachtchouk M, Bolinger M, Litingtung Y, Robertson EK, Cooper MK, Gaffield W, Westphal H, Beachy PA, et al. 1999. Essential role for Sonic hedgehog during hair follicle morphogenesis. *Dev Biol* **205:** 1–9. doi:10.1006/dbio.1998.9103

Clevers H. 2013. The intestinal crypt, a prototype stem cell compartment. *Cell* **154:** 274–284. doi:10.1016/j.cell.2013.07.004

Dassule HR, Lewis P, Bei M, Maas R, McMahon AP. 2000. Sonic hedgehog regulates growth and morphogenesis of the tooth. *Development* **127:** 4775–4785. doi:10.1242/dev.127.22.4775

Driever W, Nüsslein-Volhard C. 1988. The bicoid protein determines position in the *Drosophila* embryo in a concentration-dependent manner. *Cell* **54:** 95–104. doi:10.1016/0092-8674(88)90183-3

Fu J, Hsu W. 2013. Epidermal Wnt controls hair follicle induction by orchestrating dynamic signaling crosstalk between the epidermis and dermis. *J Invest Dermatol* **133:** 890–898. doi:10.1038/jid.2012.407

Gao P, Postiglione MP, Krieger TG, Hernandez L, Wang C, Han Z, Streicher C, Papusheva E, Insolera R, Chugh K, et al. 2014. Deterministic progenitor behavior and unitary production of neurons in the neocortex. *Cell* **159:** 775–788. doi:10.1016/j.cell.2014.10.027

Glover JD, Wells KL, Matthäus F, Painter KJ, Ho W, Riddell J, Johansson JA, Ford MJ, Jahoda CAB, Klika V, et al. 2017. Hierarchical patterning modes orchestrate hair follicle morphogenesis. *PLoS Biol* **15:** e2002117. doi:10.1371/journal.pbio.2002117

Goncalves AN, Correia-Pinto J, Nogueira-Silva C. 2020. ROBO2 signaling in lung development regulates SOX2/SOX9 balance, branching morphogenesis and is dysregulated in nitrofen-induced congenital diaphragmatic hernia. *Respir Res* **21:** 302. doi:10.1186/s12931-020-01568-w

Greenfeld H, Lin J, Mullins MC. 2021. The BMP signaling gradient is interpreted through concentration thresholds in dorsal-ventral axial patterning. *PLoS Biol* **19:** e3001059. doi:10.1371/journal.pbio.3001059

Gregor T, Wieschaus EF, McGregor AP, Bialek W, Tank DW. 2007. Stability and nuclear dynamics of the bicoid morphogen gradient. *Cell* **130:** 141–152. doi:10.1016/j.cell.2007.05.026

Gritli-Linde A, Hallberg K, Harfe BD, Reyahi A, Kannius-Janson M, Nilsson J, Cobourne MT, Sharpe PT, McMahon AP, Linde A. 2007. Abnormal hair development and apparent follicular transformation to mammary gland in the absence of hedgehog signaling. *Dev Cell* **12:** 99–112. doi:10.1016/j.devcel.2006.12.006

Gupta K, Levinsohn J, Linderman G, Chen D, Sun TY, Dong D, Taketo MM, Bosenberg M, Kluger Y, Choate K, et al. 2019. Single-cell analysis reveals a hair follicle dermal niche molecular differentiation trajectory that begins prior to morphogenesis. *Dev Cell* **48:** 17–31.e6. doi:10.1016/j.devcel.2018.11.032

Guzmán-Palma P, Contreras EG, Mora N, Smith M, González-Ramírez MC, Campusano JM, Sierralta J, Hassan BA, Oliva C. 2021. Slit/robo signaling regulates multiple stages of the development of the *Drosophila* motion detection system. *Front Cell Dev Biol* **9:** 612645. doi:10.3389/fcell.2021.612645

Hamilton TG, Klinghoffer RA, Corrin PD, Soriano P. 2003. Evolutionary divergence of platelet-derived growth factor α receptor signaling mechanisms. *Mol Cell Biol* **23:** 4013–4025. doi:10.1128/MCB.23.11.4013-4025.2003

Hao Y, Hao S, Andersen-Nissen E, Mauck WM, Zheng S, Butler A, Lee MJ, Wilk AJ, Darby C, Zager M, et al. 2021. Integrated analysis of multimodal single-cell data. *Cell* **184:** 3573–3587.e29. doi:10.1016/j.cell.2021.04.048

Harada N, Tamai Y, Ishikawa T, Sauer B, Takaku K, Oshima M, Taketo MM. 1999. Intestinal polyposis in mice with a dominant stable mutation of the β-catenin gene. *EMBO J* **18:** 5931–5942. doi:10.1093/emboj/18.21.5931

Hardy MH. 1992. The secret life of the hair follicle. *Trends Genet* **8:** 55–61. doi:10.1016/0168-9525(92)90350-D

Huh SH, Närhi K, Lindfors PH, Häärä O, Yang L, Ornitz DM, Mikkola ML. 2013. Fgf20 governs formation of primary and secondary dermal condensations in developing hair follicles. *Genes Dev* **27:** 450–458. doi:10.1101/gad.198945.112

Jeong J, Mao J, Tenzen T, Kottmann AH, McMahon AP. 2004. Hedgehog signaling in the neural crest cells regulates the patterning and growth of facial primordia. *Genes Dev* **18:** 937–951. doi:10.1101/gad.1190304

Kicheva A, Bollenbach T, Wartlick O, Jülicher F, Gonzalez-Gaitan M. 2012. Investigating the principles of morphogen gradient formation: from tissues to cells. *Curr Opin Genet Dev* **22:** 527–532. doi:10.1016/j.gde.2012.08.004

Lander AD, Nie Q, Wan FY. 2002. Do morphogen gradients arise by diffusion? *Dev Cell* **2:** 785–796. doi:10.1016/S1534-5807(02)00179-X

Millar SE. 2002. Molecular mechanisms regulating hair follicle development. *J Invest Dermatol* **118:** 216–225. doi:10.1046/j.0022-202x.2001.01670.x

Mok KW, Saxena N, Heitman N, Grisanti L, Srivastava D, Muraro MJ, Jacob T, Sennett R, Wang Z, Su Y, et al. 2019. Dermal condensate niche fate specification occurs prior to formation and is placode progenitor dependent. *Dev Cell* **48:** 32–48.e5. doi:10.1016/j.devcel.2018.11.034

Morita R, Sanzen N, Sasaki H, Hayashi T, Umeda M, Yoshimura M, Yamamoto T, Shibata T, Abe T, Kiyonari H, et al. 2021. Tracing the origin of hair follicle stem cells. *Nature* **594:** 547–552. doi:10.1038/s41586-021-03638-5

Nestorowa S, Hamey FK, Pijuan Sala B, Diamanti E, Shepherd M, Laurenti E, Wilson NK, Kent DG, Göttgens B. 2016. A single-cell resolution map of mouse hematopoietic stem and progenitor cell differentiation. *Blood* **128:** e20–e31. doi:10.1182/blood-2016-05-716480

Ouspenskaia T, Matos I, Mertz AF, Fiore VF, Fuchs E. 2016. WNT-SHH antagonism specifies and expands stem cells prior to niche formation. *Cell* **164:** 156–169. doi:10.1016/j.cell.2015.11.058

Phan QM, Fine GM, Salz L, Herrera GG, Wildman B, Driskell IM, Driskell RR. 2020. Lef1 expression in fibroblasts maintains developmental potential in adult skin to regenerate wounds. *eLife* **9:** e60066. doi:10.7554/eLife.60066

Qu R, Gupta K, Dong D, Jiang Y, Landa B, Saez C, Strickland G, Levinsohn J, Weng PL, Taketo MM, et al. 2022. Decomposing a deterministic path to mesenchymal niche formation by two intersecting morphogen gradients. *Dev Cell* **57:** 1053–1067.e5. doi:10.1016/j.devcel.2022.03.011

Qu R, Cheng X, Sefik E, Stanley JS Iii, Landa B, Strino F, Platt S, Garritano J, Odell ID, Coifman R, et al. 2024. Gene trajectory inference for single-cell data by optimal transport metrics. *Nat Biotechnol* **43:** 258–268. doi:10.1038/s41587-024-02186-3

Reddy S, Andl T, Bagasra A, Lu MM, Epstein DJ, Morrisey EE, Millar SE. 2001. Characterization of Wnt gene expression in developing and postnatal hair follicles and identification of Wnt5a as a target of Sonic hedgehog in hair follicle morphogenesis. *Mech Dev* **107:** 69–82. doi:10.1016/S0925-4773(01)00452-X

Roelink H, Porter JA, Chiang C, Tanabe Y, Chang DT, Beachy PA, Jessell TM. 1995. Floor plate and motor neuron induction by different concentrations of the amino-terminal cleavage product of sonic hedgehog autoproteolysis. *Cell* **81:** 445–455. doi:10.1016/0092-8674(95)90397-6

Rompolas P, Deschene ER, Zito G, Gonzalez DG, Saotome I, Haberman AM, Greco V. 2012. Live imaging of stem cell and progeny behaviour in physiological hair-follicle regeneration. *Nature* **487:** 496–499. doi:10.1038/nature11218

St-Jacques B, Dassule HR, Karavanova I, Botchkarev VA, Li J, Danielian PS, McMahon JA, Lewis PM, Paus R, McMahon AP. 1998. Sonic hedgehog signaling is essential for hair development. *Curr Biol* **8:** 1058–1069. doi:10.1016/S0960-9822(98)70443-9

Sun Q, Lee W, Hu H, Ogawa T, De Leon S, Katehis I, Lim CH, Takeo M, Cammer M, Taketo MM, et al. 2023. Dedifferentiation maintains melanocyte stem cells in a dynamic niche. *Nature* **616:** 774–782. doi:10.1038/s41586-023-05960-6

te Welscher P, Zuniga A, Kuijper S, Drenth T, Goedemans HJ, Meijlink F, Zeller R. 2002. Progression of vertebrate limb development through SHH-mediated counteraction of GLI3. *Science* **298:** 827–830. doi:10.1126/science.1075620

van Amerongen R, Bowman AN, Nusse R. 2012. Developmental stage and time dictate the fate of Wnt/β-catenin-responsive stem cells in the mammary gland. *Cell Stem Cell* **11:** 387–400. doi:10.1016/j.stem.2012.05.023

Vokes SA, Ji H, Wong WH, McMahon AP. 2008. A genome-scale analysis of the *cis*-regulatory circuitry underlying sonic hedgehog-mediated patterning of the mammalian limb. *Genes Dev* **22:** 2651–2663. doi:10.1101/gad.1693008

Wang DH, Clemons NJ, Miyashita T, Dupuy AJ, Zhang W, Szczepny A, Corcoran-Schwartz IM, Wilburn DL, Montgomery EA, Wang JS, et al. 2010. Aberrant epithelial–mesenchymal Hedgehog signaling characterizes Barrett's metaplasia. *Gastroenterology* **138:** 1810-1822. doi:10.1053/j.gastro.2010.01.048

Wolpert L. 1969. Positional information and the spatial pattern of cellular differentiation. *J Theor Biol* **25:** 1–47. doi:10.1016/S0022-5193(69)80016-0

Woo WM, Zhen HH, Oro AE. 2012. Shh maintains dermal papilla identity and hair morphogenesis via a Noggin-Shh regulatory loop. *Genes Dev* **26:** 1235–1246. doi:10.1101/gad.187401.112

Yu G, He QY. 2016. ReactomePA: an R/Bioconductor package for reactome pathway analysis and visualization. *Mol Biosyst* **12:** 477–479. doi:10.1039/C5MB00663E

Zhang Y, Tomann P, Andl T, Gallant NM, Huelsken J, Jerchow B, Birchmeier W, Paus R, Piccolo S, Mikkola ML, et al. 2009. Reciprocal requirements for EDA/EDAR/NF-κB and Wnt/β-catenin signaling pathways in hair follicle induction. *Dev Cell* **17:** 49–61. doi:10.1016/j.devcel.2009.05.011

Zhao J, Jaffe A, Li H, Lindenbaum O, Sefik E, Jackson R, Cheng X, Flavell RA, Kluger Y. 2021. Detection of differentially abundant cell subpopulations in scRNA-seq data. *Proc Natl Acad Sci* **118:** e2100293118. doi:10.1073/pnas.2100293118